International Journal of Fatigue 110 (2018) 172–185

Contents lists available at ScienceDirect

International Journal of Fatigue

journal homepage: www.elsevier.com/locate/ijfatigue

Crack growth analysis in welded and non-welded T-joints based on lock-in digital image correlation and thermoelastic stress analysis

Daoyun Chen[a,*], Shouguang Sun[a], J.M. Dulieu-Barton[b], Qiang Li[a], Wenjing Wang[a]

[a] Key Laboratory of Vehicle Advanced Manufacturing, Measuring and Control Technology (Beijing Jiaotong University), Ministry of Education, PR China
[b] Faculty of Engineering and the Environment, University of Southampton, SO17 1BJ, United Kingdom

ARTICLE INFO

Keywords:
Crackgrowth analysis
Digital image correlation
Thermoelastic stress analysis
Stress intensity factor
Extended finite element method

ABSTRACT

The method based on the digital image correlation (DIC) technique and thermoelastic stress analysis (TSA) is proposed to monitor the crack propagation process of T-joint specimens during the fatigue test. The lock-in amplifier is used to process DIC speckle pattern images while the specimen is dynamically loaded. The lock-in algorithm uses the fact that lock-in amplifier can be able to detect very small signal change within the measurement noise, which is often used in TSA. Using appropriate post-processing method, both the crack lengths and the stress intensity factors (SIF) can be evaluated in function of the number of fatigue cycles. The tests on non-welded T-joint specimens and welded T-joint specimens in two types of test rigs will be presented in the paper. All of the achieved results were validated by employing extended finite element method (XFEM) performed with ANSYS software.

1. Introduction

The use of full-field optical techniques has grown fast over the past several decades due to the progress in digital camera and infrared camera performance and increased computational power. The full-field nature enables the identifying of strain concentrations and damage more accurate. DIC and TSA have become the most popular of these optical measurement techniques. DIC is based on the correlation algorithm to track surface patterns and hence obtain the displacements and strains that occur during loading. Most of the application of DIC has been carried out on structures under static load. La Rosa et al. [1] used DIC to correct the thermoelastic curves in static tests. Recently several researchers explored the application of DIC in fatigue tests. Kirugulige et al. [2] combined the DIC technique with a rotating mirror-type high-speed digital camera for transient crack growth study. The dynamic crack growth behavior of a polymeric beam which was subjected to impact loading was researched using the developed methodology. Chao [3] used DIC to obtain the deformation fields around a crack tip from photographic films recorded by a high-speed camera. The SIF was also calculated using the in-plane displacements and strains. Giancarlo et al. [4] used DIC to obtain the SIF via experimental J-integral evaluations in a compact-tension specimen subjected to mode I loading conditions. The J-integral was computed over an arbitrary but elastic contour path enclosing the crack tip. Good agreement can be found between the calculated SIF and the analytical values obtained from ASTM equation. However, these applications are all based on the use of high-speed cameras which also bring difficulties: the DIC evaluation algorithm must be applied carefully to process the image sequences since many images are obtained. In addition, the cost of high-speed DIC cameras is quite high. Fruehmann et al. [5] used a lock-in amplifier in DIC to monitor crack growth process during fatigue tests without using expensive high-speed cameras. It is found that the low frame rate capability of standard digital cameras does not present an unsurmountable challenge in the application of DIC at high loading rates. TSA is based on the thermoelastic effect where a temperature change induced by cyclic loading can be directly related to the change in stresses [6]. An infrared detector is often used to obtain the surface temperature change, which has been proved to be a useful tool to evaluate the local effects such as damage. Farahani et al. [7]. studied the experimental determination of SIF using TSA for a compact tension specimen during a fatigue test. The stress field obtained with computational modelling and finite element method were used as a comparison. The results obtained with different techniques show a satisfied agreement. Yates et al. [8]. researched the crack paths under mixed mode loading using TSA. It is found that the direction of fatigue crack propagation may be governed more strongly by directionality of crack tip plasticity rather than by the magnitude of elastic stress field alone. Apart from DIC and TSA, synchrotron radiation X-ray computed microtomography (SR-μCT), a newly developed method for monitoring crack growth progress, has been applying to fatigue analysis on structures. Withers et al. [9]

* Corresponding author.
E-mail address: 13116326@bjtu.edu.cn (D. Chen).

https://doi.org/10.1016/j.ijfatigue.2018.01.020
Received 10 November 2017; Received in revised form 21 January 2018; Accepted 22 January 2018

employed SR-μCT to study internal damage accumulation and evolution in structural materials. The method permits 3D imaging of damage accumulation and the time lapse imaging of damage evolution for environmental and mechanical loading and provides quantitative information about key fracture mechanics parameters.

In this paper, the crack growth mechanism of welded T-joints and non-welded T-joints in two types of test rigs is studied based on lock-in DIC technique and TSA. ANSYS software was used to design the test rig, decide the experimental load and validate results.

2. Theoretical background

2.1. DIC and lock-in amplifier

DIC is a kind of full-field optical technique which enables areal inspection of strains making them ideally suited for identifying strain concentrations and/or damage. In order to obtain whole displacement field and strain field, image comparison of the specimens coated with a random speckle pattern is needed. The speckle pattern of the undeformed specimen is compared with the images of deformed specimen. The pattern matching is based on obtaining a maximum correlation between subsets of the image in the deformed and undeformed states (see Fig. 1). The correlation function as shown in Eq. (1) is used for matching purpose. The displacement of the centre of pixel subset is returned when the best match is identified. The strain fields are obtained from the gradients of smoothed displacement fields using a numerical differentiation scheme:

$$C(u,v) = \frac{\sum_{i=1}^{m}\sum_{j=1}^{m}[f(x_i,y_i)-\overline{f}\,][g(x_i',y_i')-\overline{g}]}{\sqrt{\sum_{i=1}^{m}\sum_{j=1}^{m}[f(x_i,y_i)-\overline{f}\,]^2}\sqrt{\sum_{i=1}^{m}\sum_{j=1}^{m}[g(x_i',y_i')-\overline{g}]^2}} \tag{1}$$

where

$$x' = x + u_0 + \frac{\partial u}{\partial x}\mathrm{d}x + \frac{\partial u}{\partial y}\mathrm{d}y \quad y' = y + v_0 + \frac{\partial v}{\partial x}\mathrm{d}x + \frac{\partial v}{\partial y}\mathrm{d}y \tag{2}$$

$\overline{f}$ is the mean intensity value of reference subset; $\overline{g}$ is the mean intensity value of deformed subset; m is the width of the subset in pixels; u_0 and v_0 are translations of the centre of the subset in the x and y directions.

Most of the application of DIC has been carried out on structures under static load. For fatigue tests, they are typically time-consuming and accordingly expensive. In order to elicit more information about the structural behaviour and enable more efficient testing approaches, a full-field technique such as DIC is highly desirable. Many researchers have successfully enabled DIC for dynamic tests. Wu [10] made the stroboscopic lighting synchronised to the loading. Risbet [11] directly synchronised the image trigger to the loading cycle. However, the set-up of these methods is very complex and relatively expensive. In addition, they do not provide any improvement in terms of strain or spatial resolution compared to the standard static approach. Since the capture frequency of DIC camera is very low compared to the load frequency, it is hard to reach the requirement of Shannon's sampling theorem [12] which requires the sampling frequency is greater than two times the maximum frequency contained in the measurement signal (the Nyquist or critical frequency).

In order to solve this problem, the lock-in amplifier is employed in this paper. The lock-in amplifier is established for obtaining the amplitude and phase of small sinusoidal signals embedded within a noisy signal [13–15]. The lock-in amplifier multiplies an input signal by a reference signal and integrates the result over a number of periods. This produces a DC level proportional to the amplitude of only that component of the input signal at the same frequency as the reference signal [16]. The lock-in amplifier is phase sensitive, hence a two-phase lock-in amplifier is applied that uses not only the reference signal but also its quadrature to output an X and a Y component from which the amplitude and phase angle between the input and reference signals can be obtained:

$$X = \frac{1}{N/2}\sum_{i=1}^{N} f(t_i)\sin(\omega t_i + \phi) \tag{3}$$

$$Y = \frac{1}{N/2}\sum_{i=1}^{N} f(t_i)\cos(\omega t_i + \phi) \tag{4}$$

$$A = \sqrt{X^2 + Y^2} \tag{5}$$

$$\phi = \tan^{-1}(Y/X) \tag{6}$$

where N is the number of samples, i is the sample number, $f(t_i)$ is the input signal as a function of time t, $\sin(\omega t_i + \phi)$ is the reference signal with frequency ω and phase ϕ, $\cos(\omega t_i + \phi)$ is the quadrature of the reference signal and A is the amplitude.

It is worth noting that the reference signal must have a mean of zero and an amplitude of 1 in order not to scale the results. This was done by generating a normalised reference signal according to:

$$r_{norm}(t_i) = \frac{r(t_i)-\bar{r}}{A_r} \tag{7}$$

where $r(t_i)$ is the reference signal, r_{norm} is the normalised reference signal, $\bar{r}$ is the mean of the reference signal and A_r is the amplitude of the reference signal obtained using Fast Fourier Transform (FFT). The quadrature was obtained as the imaginary part of a Hilbert transform of the normalised reference signal. Fig. 2 shows a typical flowchart of the procedure for lock-in DIC.

2.2. TSA

Thermoelastic stress analysis is a full-field stress measurement technique based on the thermoelastic effect. This effect states that any substance in nature experiences changes in its temperature when its volume is changed: compressive loads cause an increase in temperature while tensile load leads to a decrease in temperature. Hence, a cyclic change in temperature can be inferred if applying a cyclic load to the

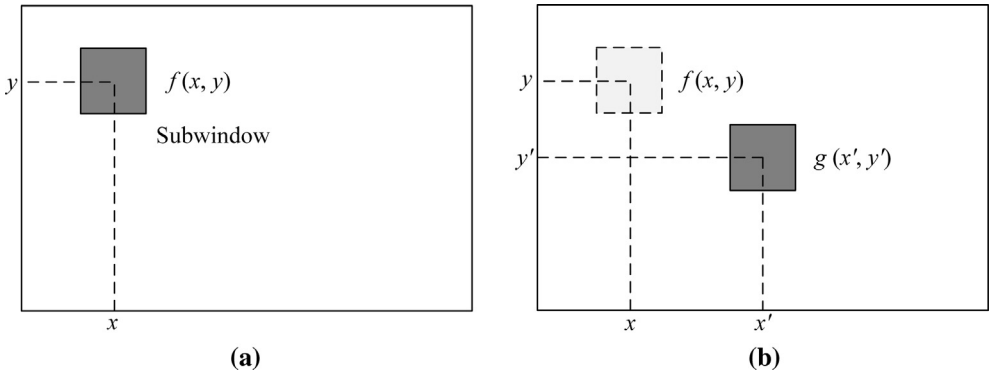

Fig. 1. Schematic of subset matching DIC. (a) Undeformed, (b) deformed.

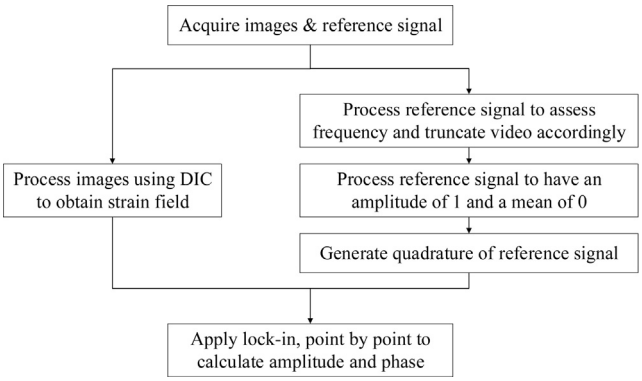

Fig. 2. Lock-in processing flow.

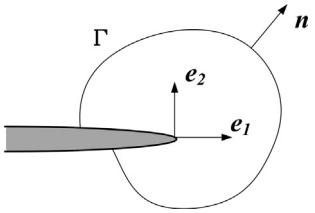

Fig. 3. Coordinate System of Crack Tip.

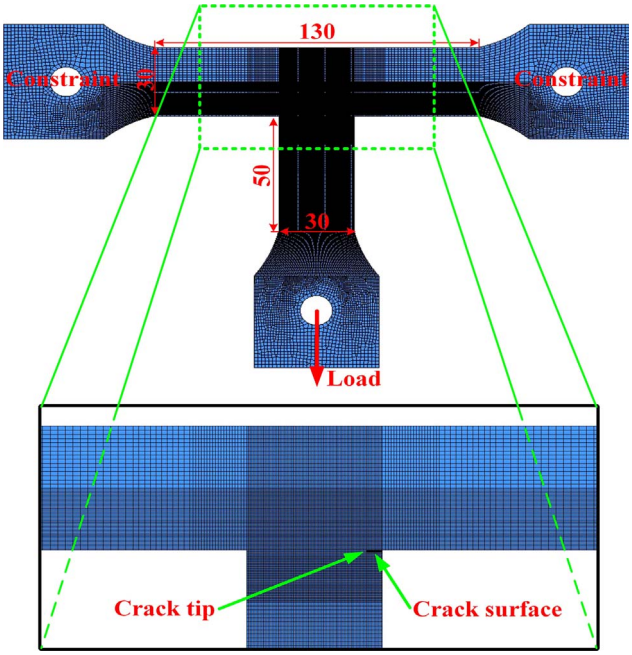

Fig. 4. Finite Element Model and Main Dimensions under load type 1.

specimen. Generally speaking, the temperature variations are normally very small under elastic conditions. Using high precision infrared detectors, the small temperature change can be quantified. In thermoelastic theory, it is considered that the temperatures variations experienced by the cyclically loaded material are proportional to the sum of principal stresses under adiabatic and reversible conditions. The relation between the change in temperature and the stress range of a linear elastic and homogeneous material can be written as:

$$\Delta T = \frac{-\alpha T}{\rho C_p}\Delta(\sigma_1 + \sigma_2) \tag{8}$$

where α is the coefficient of thermal expansion, T is the absolute temperature of the material, ρ is material density, C_p is the specific heat at constant pressure and σ_1 and σ_2 are principal stresses.

Acquisition systems used in TSA are based on a correlation in frequency, amplitude and phase of the detected signal with a reference signal coming from the loading system. TSA provides a signal proportional to the peak-to-peak variation in temperature during the peak-to-peak variation of the sum of principal stress. The phase means the angular shift between the thermoelastic and the reference signal. The phase is normally constant unless adiabatic conditions are not achieved [17].

3. Numerical approach

It is well known that XFEM is one of the most effective tools for computing fatigue life in 2D fracture models. In order to decide the load value used in fatigue experiment and to get the theory result of crack growth, XFEM is always very necessary. In this paper, ANSYS 17.1 commercial software was used for finite element simulation.

3.1. Calculation of SIF

The domain integral representation of the J-integral [18] is given by

$$J = \int_A \left[\sigma_{ij}\frac{\partial u_j}{\partial x_i} - w\delta_{ij}\right]\frac{\partial q}{\partial x_i}dA \tag{9}$$

where

σ_{ij} = Stress tensor
u_j = Displacement vector
w = Strain energy density
δ_{ij} = Kronecker delta
x_i = Coordinate axis
q = Crack-extension vector

The direction of q is the simple x-axis of the local coordinate system ahead of the crack tip (Fig. 3). The q vector is chosen as zero at nodes along the contour Γ, and is a unit vector for all nodes inside **Γ** except the midside nodes, if there are any, that are directly connected to Γ.With the value of J-integral, the SIF can then be calculated by the following formula [19],

$$K = \sqrt{\frac{EJ}{1-\upsilon^2}} \tag{10}$$

where

E = Young's modulus,
J = J-integral,
ϑ = Poisson's ratio.

Table 1
Maximum load and minimum load evaluated from threshold SIF and critical SIF.

Load/N	K_I/MPa$\sqrt{m}$	K_{II}/MPa$\sqrt{m}$	K_{equi}/MPa$\sqrt{m}$	K_{th}/MPa$\sqrt{m}$	K_c/MPa$\sqrt{m}$	m	$C/\frac{\text{mm / cycle}}{(\text{MPa}\cdot\sqrt{\text{m}})^m}$
220	3.4	−0.3	3.4	3.4	68	3.05	3.58E−10
4140	67.1	−6.5	68				

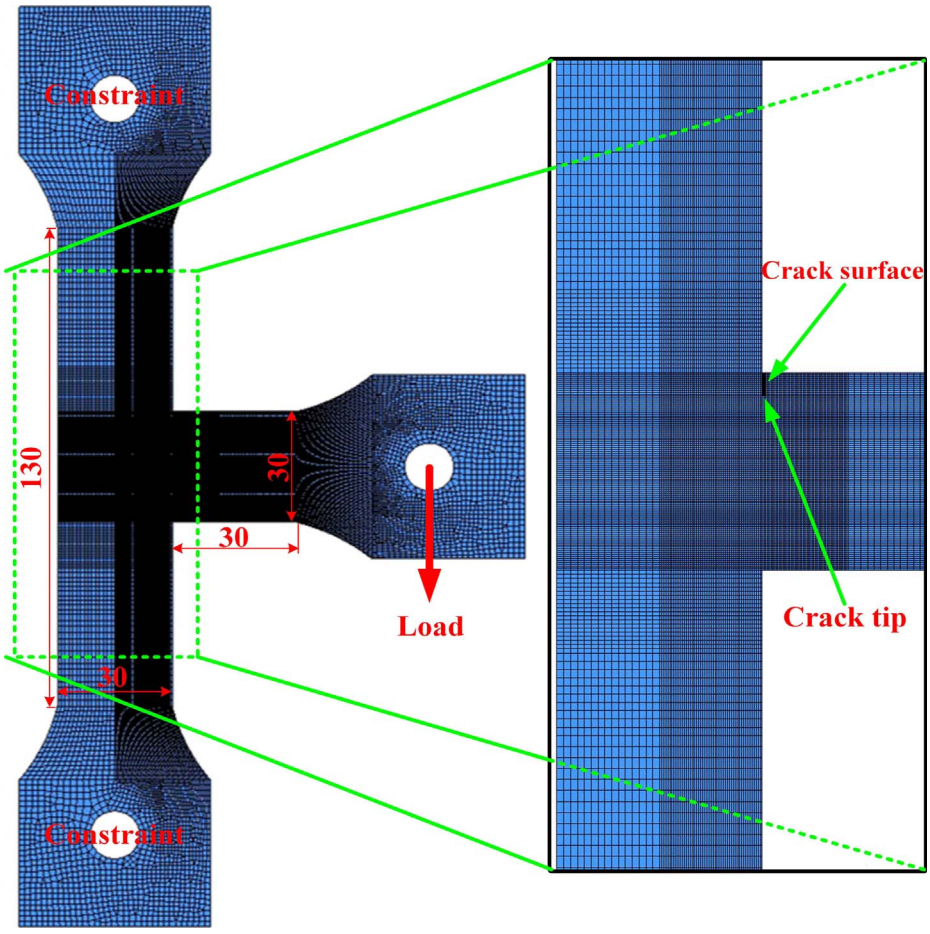

Fig. 5. Finite Element Model and Main Dimensions under load type 2.

Table 2
Maximum load and minimum load evaluated from threshold SIF and critical SIF.

Load/kN	K_I/MPa$\sqrt{m}$	K_{II}/MPa$\sqrt{m}$	K_{equi}/MPa$\sqrt{m}$	K_{th}/MPa$\sqrt{m}$	K_c/MPa$\sqrt{m}$	m	$C/\frac{\text{mm / cycle}}{(\text{MPa}\cdot\sqrt{\text{m}})^m}$
1.6	3.1	−1.6	3.4	3.4	68	3.05	3.58E−10
30	60.8	−30.8	68				

3.2. Crack propagation law

The crack growth simulation in ANSYS is based on XFEM which offers an approach for simulating fatigue crack propagation without resorting to modelling the cracks or remeshing the crack tip regions as the crack propagates. This approach is based on Paris' Law and only linear elastic isotropic materials are supported. In addition, large-deflection, finite-rotation effects, crack tip plasticity effects, crack tip closure effects are ignored.The crack growth rate [20] is defined as

$$\frac{da}{dn} = f(\Delta K, R) \tag{11}$$

where

a = crack length,
n = number of cycles,
$\Delta K = K_{max} - K_{min,}$
R = load ratio.

The crack growth simulation is restricted to the linear region of Paris' Law:

$$\frac{da}{dn} = C(\Delta K)^m \tag{12}$$

For practical structures, the crack growth usually involves mixed-mode fracture. So the stress intensity factor range can be modified as [21]:

$$\Delta K_{eqv} = \frac{1}{2}\cos\left(\frac{\theta}{2}\right)[\{\Delta K_I(1+\cos\theta)\} - 3\Delta K_{II}\sin\theta] \tag{13}$$

where the direction of crack propagation is defined using the maximum circumferential stress criterion:

$$\theta = \cos^{-1}\frac{3(K_I)_{max} + (K_I)_{max}\sqrt{(K_I)^2_{max} + 8(K_{II})^2_{max}}}{(K_I)^2_{max} + 9(K_{II})^2_{max}} \tag{14}$$

3.3. Fatigue crack growth simulation

In order to perform fatigue crack growth simulation in ANSYS, the constants of Paris' Law must be specified. On one hand, different materials have different Paris' Law constants, on the other hand, different load types and fracture modes can also lead to different Paris' Law constants [22]. That is to say, the best way to get Paris' Law constants is by experiment. In order to evaluate the load for threshold SIF and

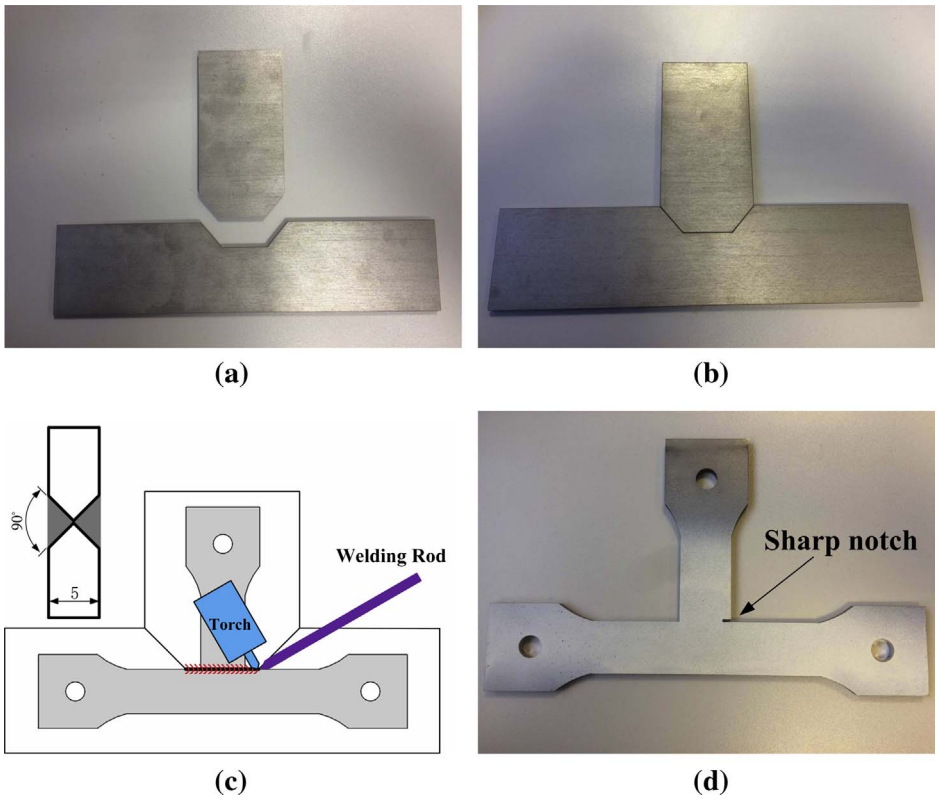

Fig. 6. Test rig 1 and its parts. (a) Test rig 1, (b) part 1, (c) part 2 and (d) part 3.

Table 3
Chemical compositions of 316L stainless steel.

Element (%)	C	Ni	Cr	Mn	P	S	Si	Mo	N
316L	0.02	11.21	17.38	1.86	0.027	0.0054	0.51	2.36	0.038

critical SIF approximately, the Paris' Law constants from a literature [23] are introduced in the simulation since both of the materials in the simulation and the literature are the same. The precise constants will be got after experiments which will be used in simulation again to correct the simulation result. It is well known that the element size can affect the accuracy of simulation results. When the element size decreases, the precision usually increases [24]. However, there is always a threshold element size. When the element size is lower than the threshold value, the simulation precision will not be improved obviously. In order to determine the best element size in this study, two element sizes around the crack tip were selected as 1 and 0.1 respectively. The later simulation found that the change rates of maximum values including the sum of principal stresses change, the displacement change and SIF change et al. were less than 0.5%. Since the computational results are insensitive when changing the element size from 1 to 0.1, the actual element size near the crack tip selected in the simulation is 0.1. The size of the outer layer elements near the crack tip are gradually increasing to raise the solution speed.

3.3.1. Load type 1

Load type 1 is also a frequently used load type. The finite element model and main dimensions of the T-joint under load type 1 is shown in Fig. 4. The length of the precrack is 5 mm and the mesh around crack tip is refined to make the result precise. The element type is chosen as plane 182 which is necessary for the XFEM based fatigue crack growth simulation in ANSYS.

As we all know, on one hand, there is a threshold SIF for crack propagation. If the SIF around crack tip is smaller than threshold value K_{th}, then crack will not grow. On the other hand, there is a critical SIF K_c for crack growth. If the SIF of crack tip exceeds this value, then the crack will propagate with an extremely fast speed which should be avoided. According to the fracture mechanics theory, crack growth includes three stages: crack initiation stage, stable crack growth stage and fracture stage. The practical crack growth test should be stable, that is to say, the load applied to the specimen should not be too high or too low. One of the aims of simulation is to decide the best load in crack propagation test. In order to achieve this goal, firstly the loads when SIF equals to K_{th} and K_c should be calculated using ANSYS. The results including the necessary fracture parameters from relevant literatures [25,26] are listed in Table 1. As can be seen from Table 1, the experimental load should be selected between 220 N and 4140 N. Considering the crack propagation speed, stability and safety, the amplitude of sinusoidal load is chosen as 0.8kN with a load ratio of 0.11.

3.3.2. Load type 2

Fig. 5 shows finite element model and main dimensions of the T-joint under load type 2. It is clear that nothing is changed except the load direction. The maximum experimental load and minimum experimental load are also determined which is shown in Table 2. Considering the crack propagation speed, stability and safety, the amplitude of sinusoidal load is chosen as 2.1kN with a load ratio of 0.045.

4. Experimental studies

4.1. Specimen fabrication

There were two types of specimens used in the fatigue test. One was water jet cut from the 316L stainless steel sheet directly, the other was welded from two separate parts, which is shown in Fig. 6. The tungsten inert gas (TIG) welding technique was used to join the two plates together and then the T-shaped specimen was cut out. The reason why not welding the final shape parts directly is that the angle between web and flange could not be a right angle since welding will lead to slight deformation. The 5 mm long sharp notch on the corner of T represents the

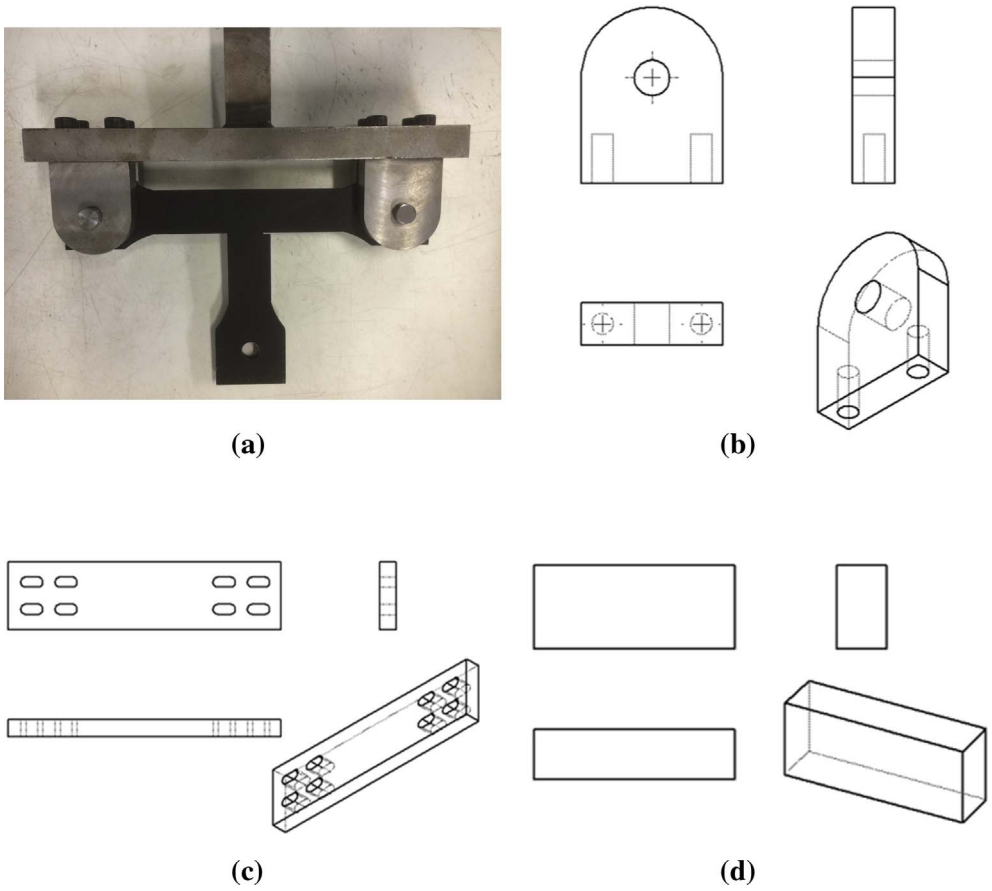

Fig. 7. Strength evaluation of the test rig in ANSYS Workbench 17.1: (a) assembly model (b) VonMises stress of the bar (c) VonMises stress of the seat (d) VonMises stress of the specimen.

initiated crack employed artificially. The material of the base metal and welding are all 316L stainless steels. Therefore, the materials ahead of the crack tip are identical in all of the T-joint specimens. The crack tip of the base metal specimen is located in the base metal. The crack tip of the welding specimen is located in the welding seam. Table 3 shows the chemical composition of 316L stainless steel [25].

4.2. Test rig design

The test rig design mainly includes three parts, that is structure design, strength checking and manufacture. The first two parts are often carried out by using softwares such as SOLIDWORKS and ANSYS. After simulation design, the test rig can then be manufactured by factories.

4.2.1. Test rig 1

Load type 1 is frequently used and easy to be applied by researchers. Fig. 7 shows the test rig designed by Angelos [27] who was in the same research group with the author. Test rig 1 consists of three parts. Part 1 and part 2 are connected with bolts whereas part 2 and part 3 are welded together. The holes in part 2 are designed in a way to allow small corrections during the compilation of the parts and the specimen. In addition, at the lower surface of part 2, a rectangular area is carved. The dimensions of that area are slightly bigger than those of part 3. This allows part 3 to fit perfectly into part 2 and keeps it vertical after welding. The material of each part is steel AISI 1016 which is chosen in a way to fit with the requirements of the experiment.

4.2.2. Test rig 2

To apply the load showed in Figs. 4 and 5, it is needed to design two test rigs which enable the specimen installation and load applying by servo-hydraulic machine. In addition, the test rigs must satisfy the requirement of strength. To make sure that the strength of the test rig is strong enough, AISI 1050 carbon steel was finally chosen since this kind of material has higher strength than 316L stainless steel. The geometry model was built using SOLIDWORKS 2016. To check the static strength of the test rig, the assembly model was imported in ANSYS Workbench 17.1 commercial software, meshed. The contact pairs were set between pins and holes. A vertical tensile load of 2kN at the end of the bar was applied and then the whole assembly model was calculated. The assembly model and VonMises stress contour plot of the test rig components can be seen from Fig. 8. The assembly model consists of a seat, a bar, three pins and the specimen. It can be seen from Fig. 8 that most of the high-stress fields focus on the transition sections. All the VonMises stresses of the test rig components are lower than the yield stress of AISI carbon steel which is 515 MPa. Hence the test rig is strong enough to hold the specimen during the experiment.

4.3. Experimental set-ups

A matt white background was sprayed on one surface of the specimen over which a matt black speckle was applied using an RS matt black aerosol spray paint. The aim was to generate a relatively high density of small speckles for DIC. The other surface of the specimen was sprayed into black for temperature detecting of infrared camera. The DIC and TSA techniques were performed on two sides of the specimen simultaneously to evaluate the crack growth process. Fig. 9 shows the DIC and TSA set-ups and the loading equipment being used in the present study. The 2D DIC system comprises an Imager E-lite CCD camera of 2491 × 2093 pixel sensor with a pixel pitch of 3.45 µm. A Nikon zoom lens of 50 mm focal length was mounted on the CCD camera. Light emitting diode (LED) lighting was used to supply adequate image contrast. A Cedip Silver 480 M infrared camera with an indium-antimonium detector (320 × 256 pixel and acquisition rate of 383 Hz) was put on the other side of the specimen to acquire

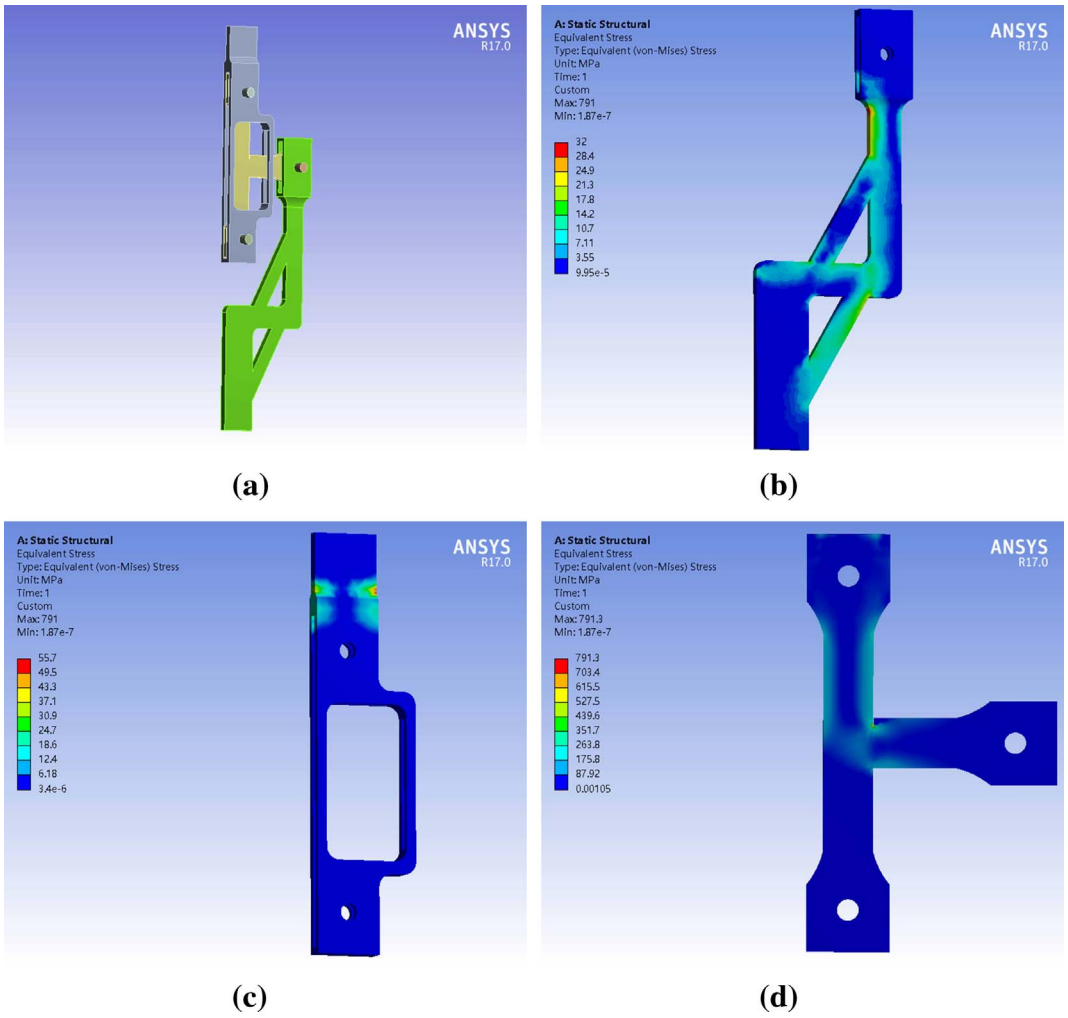

Fig. 8. Welding process of the specimen: (a) two parts for welding, (b) welding preparation, (c) TIG weld, (d) cut out specimen.

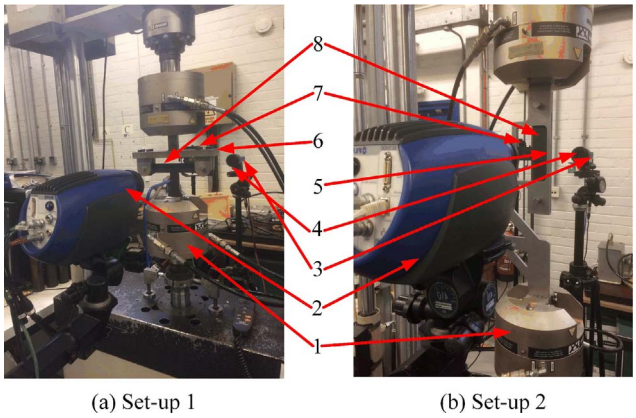

Fig. 9. Experimental set-ups for crack growth analysis: 1. Moving grip 2. infrared camera 3. DDC camera 4. zoom lens 5. test rig 2 6. test rig 1 7. light source 8. specimens.

thermoelastic images. The specimens were loaded using a computer-controlled Instron 8800 servo-hydraulic cyclic testing machine of 100 kN capacity.

It is worth noting that a number of conditions must be considered carefully since the analysis makes several assumptions about the signal that do not hold true for finite, discretely sampled signals. It is well known that the length of recorded signal is finite. As a result, the signal is truncated. To make the lock-in algorithm valid, it is, therefore, necessary to impose the condition of periodicity on the recorded signal.

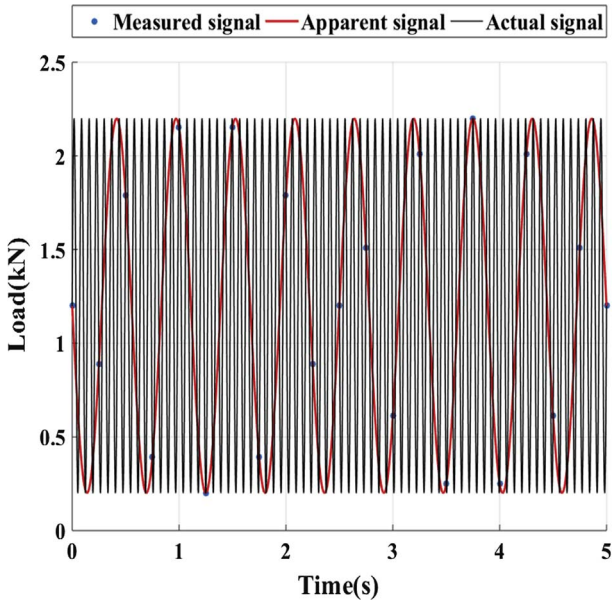

Fig. 10. Visualisation of the one complete period of an undersampled signal.

That is to say, an integer number of periods must be sampled for the recorded signal, otherwise, it will result in spectral leakage and underestimate of the signal amplitude. As a result, the frequency of

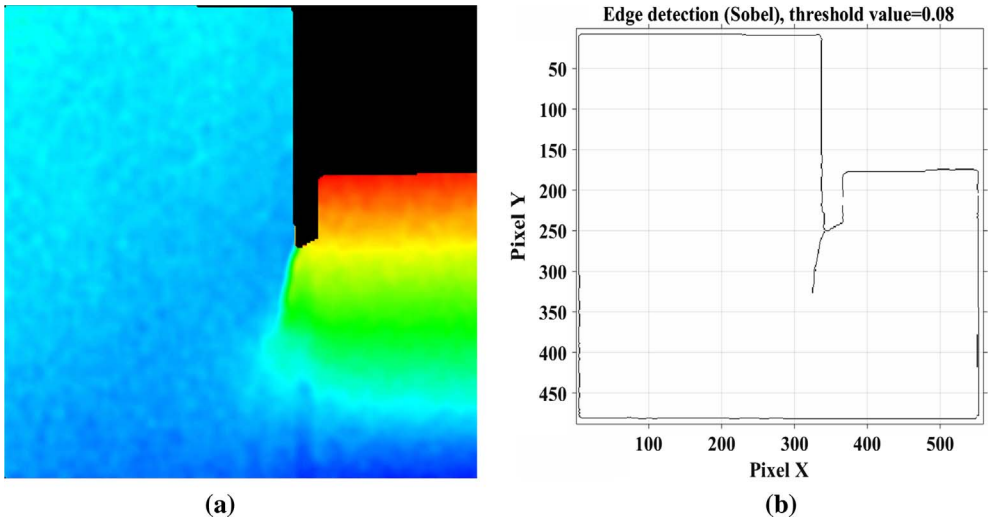

Fig. 11. Horizontal displacement range fields (21 × 21 pixel subset with 5 pixel step size) and corresponding crack detected using Matlab's Sobel algorithm.

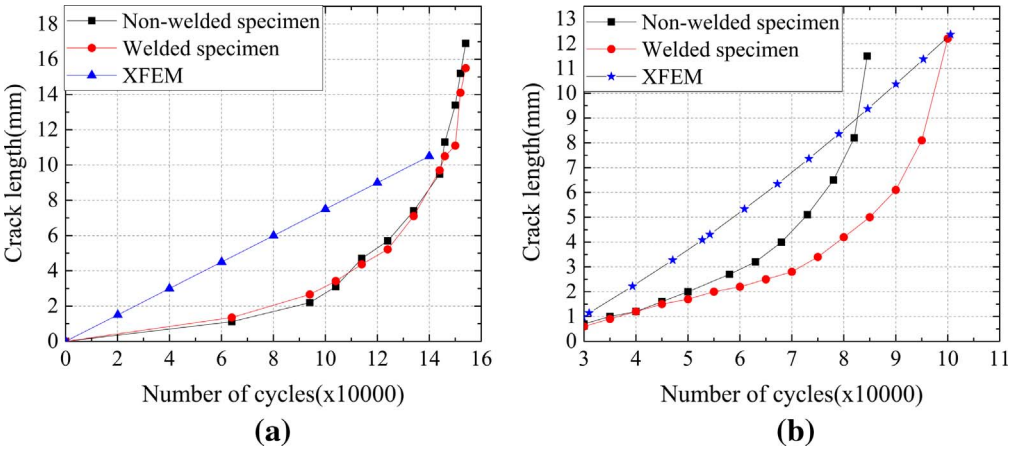

Fig. 12. Change in crack length with number of cycles, compared by the non-welded specimen, welded specimen, and XFEM. (a) Load type 1 (b) load type 2.

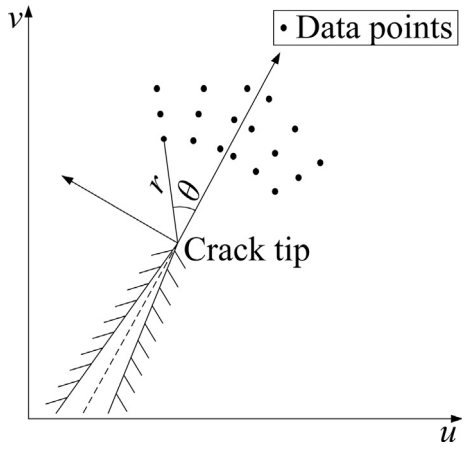

Fig. 13. Local crack tip coordinate system and data point selection used to calculate SIF.

loading and CCD image capture was set to 14.2 Hz and 4 Hz respectively. The recording time was set to 5 s for each interested cycle number. Fig. 10 shows a complete sampling periodicity of lock-in DIC.

As what is presented in Fig. 10, the actual signal has a frequency of 14.2 Hz. When sampled at 4 Hz, it gives the discrete signal represented by the blue points. These blue points coincide with a signal at 1.8 Hz. Therefore, the measured signal is treated as though it had a frequency of 1.8 Hz. Since the image capture frequency is 4 Hz, which is greater than two times the frequency of the 'measured signal', Shannon's sampling theorem is satisfied. The camera exposure time was restricted to 100 μs to minimise image blurring. Load value for each image was recorded synchronously.

5. Results and discussion

5.1. Crack length detection

To assess the crack length, the horizontal displacement fields were used in conjunction with the Sobel edge detection algorithm in Matlab. This algorithm is based on the gradients in image intensity. Edges are identified where the gradient reaches the maximum value. In order to avoid spurious measurements resulting from noise in the image, a threshold value needs to be set to define the sensitivity of the edge detection. The threshold value was selected by trial and error, increasing the value until known spurious edges detected within the specimen area were eliminated. The crack length was assessed in the vertical direction by counting the detected edge length in image pixels and multiplying by the image scale. Fig. 11(a) shows the horizontal displacement range fields at the cycle of 78,000 where a clear crack path can be seen by eyes. After using the edge detection algorithm, the identified crack can be seen from Fig. 11(b).

After detecting all of the recorded key cycles for the non-welded specimen and welded specimen using Matlab's Sobel algorithm, the final results are presented in Fig. 12 together with the XFEM result. As can be seen from Fig. 12, the crack lengths of the non-welded specimen, welded specimen, and XFEM increase with the increasing number of cycles. And it is observed that the trend between crack length and

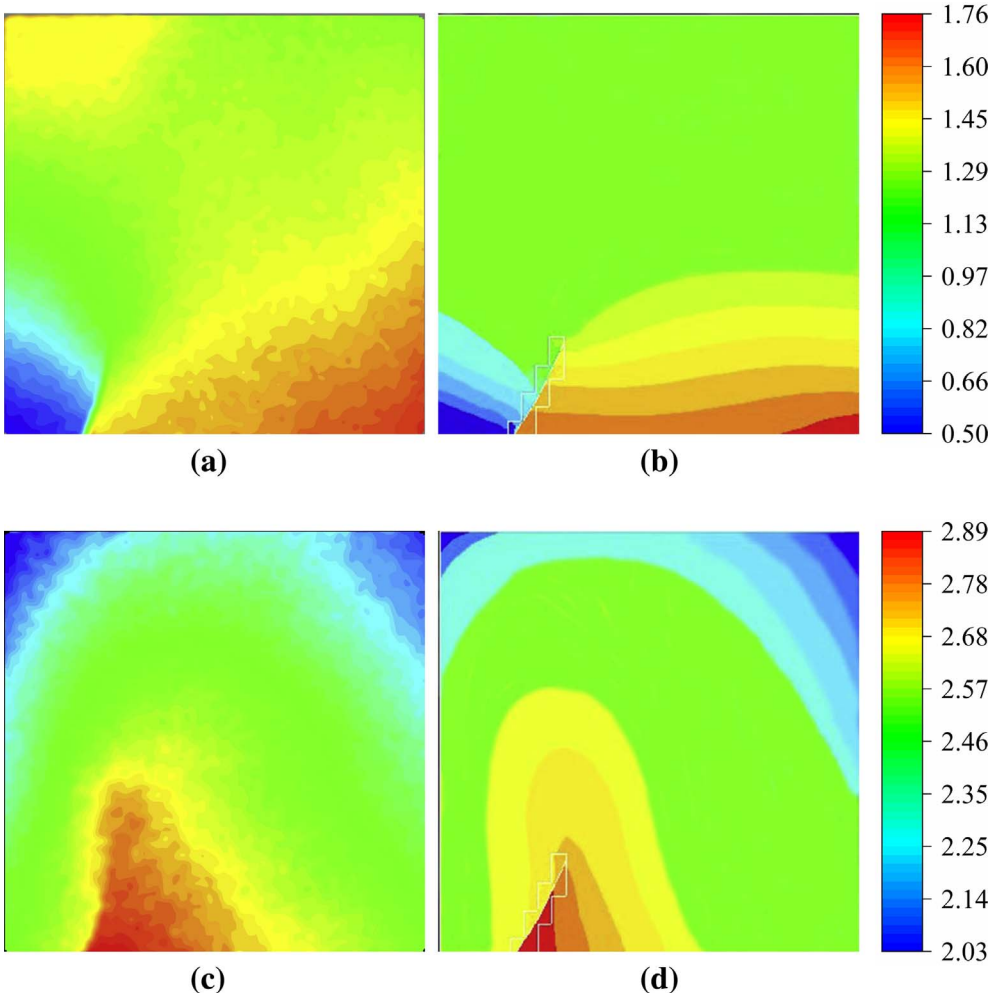

Fig. 14. Contour maps of the displacement fields in load type 1. (a) Horizontal displacement range by lock-in DIC, (b) horizontal displacement range by XFEM, (c) vertical displacement range by lock-in DIC and (d) vertical displacement range by XFEM.

number of cycles under XFEM is nearly linear since the algorithm of this approach is based on the linear crack propagation stage of Paris' law. The increasing trends of crack lengths for the non-welded specimen and welded specimen are nonlinear. For each key cycle, the crack length of the non-welded specimen is bigger than the welded one. Further, the crack length of XFEM is always bigger than the crack length of the non-welded specimen and welded specimen before cycle 80,000. After that, the crack length of non-welded specimen increases rapidly since the specimen is in the fracture stage. The fracture did not happen for the welded specimen until the cycle number reaches 100,000 which means the fatigue of the welded specimen is longer than the non-welded one.

The crack of XFEM grows faster than the non-welded specimen and the crack of welded specimen grows the slowest. After 65,000 cycles, the crack of XFEM still grows in a relatively slow and constant speed. However, the crack propagation speeds of the non-welded specimen and welded specimen increase quickly after 65,000 cycles, which means the two specimens are in the fracture stage of crack growth. It is worth noting that the crack growth rate of the non-welded specimen is always higher than the welded specimen during the whole crack propagation period.

5.2. Evaluation of SIF

According to previous studies, SIF can be evaluated from both displacement fields and principal stress fields. Since lock-in DIC can present displacement field and TSA can present principal stress field, the SIF values can then be evaluated naturally.

5.2.1. SIF evaluation approach by lock-in DIC

The displacement field ahead of a crack was first expressed as an infinite series by Williams [28]. In a plane mixed mode I and II conditions this displacement field is expressed as

$$\text{Mode I}\begin{cases} u_{\mathrm{I}} = \sum_{n=1}^{\infty} \frac{r^{\frac{n}{2}}}{2\mu} a_n \left\{ \left[\kappa + \frac{n}{2} + (-1)^n \right] \cos\frac{n\theta}{2} - \frac{n}{2}\cos\frac{(n-4)\theta}{2} \right\} \\ v_{\mathrm{I}} = \sum_{n=1}^{\infty} \frac{r^{\frac{n}{2}}}{2\mu} a_n \left\{ \left[\kappa - \frac{n}{2} - (-1)^n \right] \sin\frac{n\theta}{2} + \frac{n}{2}\sin\frac{(n-4)\theta}{2} \right\} \end{cases} \tag{15}$$

and,

$$\text{Mode II}\begin{cases} u_{\mathrm{II}} = -\sum_{n=1}^{\infty} \frac{r^{\frac{n}{2}}}{2\mu} b_n \left\{ \left[\kappa + \frac{n}{2} - (-1)^n \right] \sin\frac{n\theta}{2} - \frac{n}{2}\sin\frac{(n-4)\theta}{2} \right\} \\ v_{\mathrm{II}} = \sum_{n=1}^{\infty} \frac{r^{\frac{n}{2}}}{2\mu} b_n \left\{ \left[\kappa - \frac{n}{2} + (-1)^n \right] \cos\frac{n\theta}{2} + \frac{n}{2}\cos\frac{(n-4)\theta}{2} \right\} \end{cases} \tag{16}$$

where u and v are horizontal and vertical displacements in mode I and II. μ is the shear modulus. a and b are constants. r and θ are radial and phase distance from the crack tip. $\kappa = (3 - \nu)/(1 + \nu)$ for plane stress condition, where ν is the Poisson's ratio.

Mixed mode displacement fields can be derived by superimposing the mode I and II displacement fields. By defining $f_{n,m}(r, \theta)$, $g_{n,m}(r, \theta)$, $h_{n,m}(r, \theta)$ and $\mathrm{l}_{n,m}(r, \theta)$ (Eq. (17)) and compensating for the rigid body translations and rotations, the displacement field can be written in a matrix form:

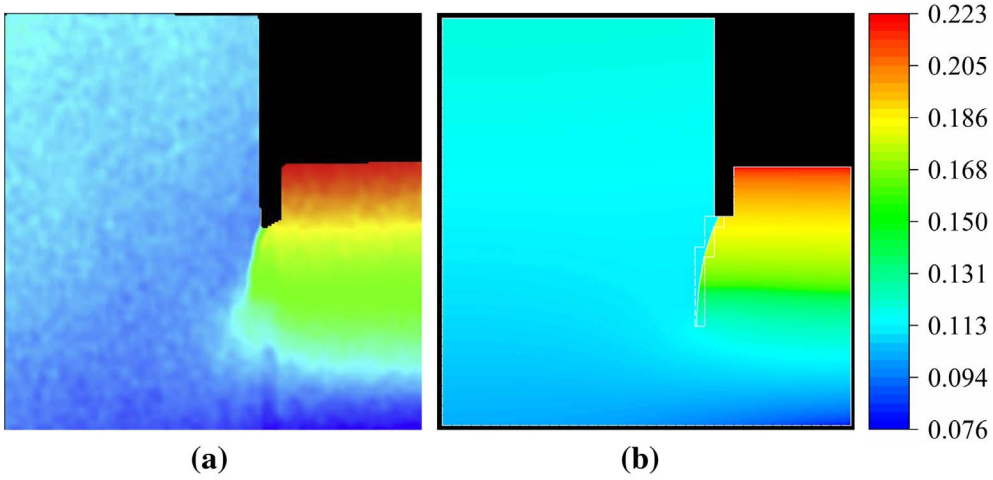

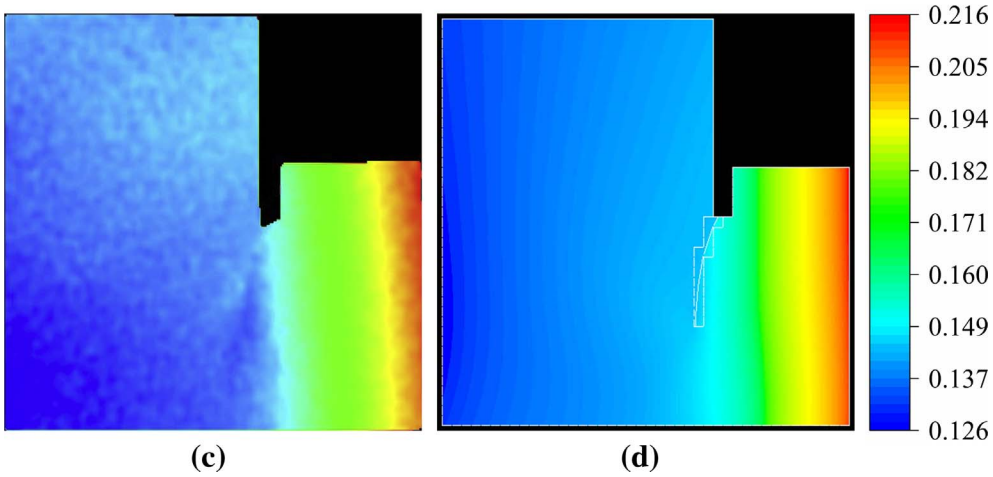

Fig. 15. Contour maps of the displacement fields in load type 2. (a) Horizontal displacement range by lock-in DIC, (b) horizontal displacement range by XFEM, (c) vertical displacement range by lock-in DIC and (d) vertical displacement range by XFEM.

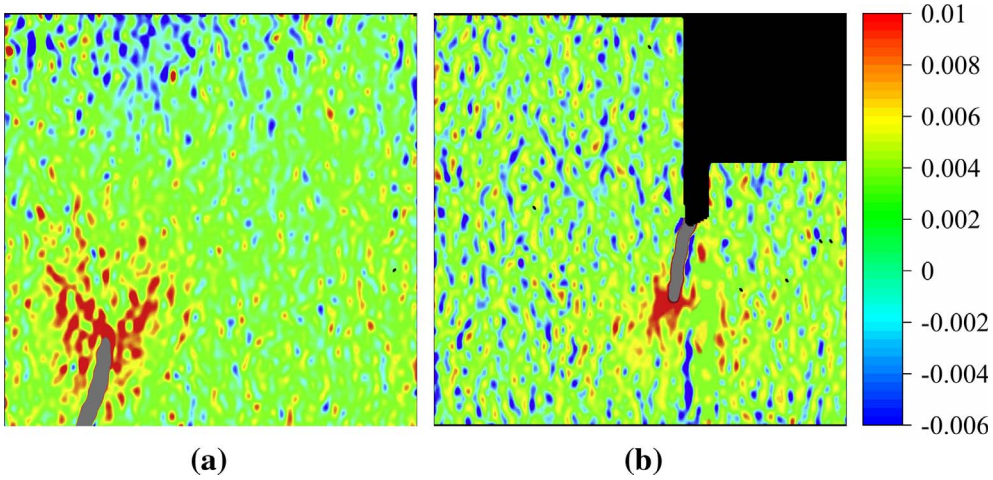

Fig. 16. ε_x strain fields (a) load type 1, (b) load type 2.

$$
\begin{aligned}
f_{n,m} &= \frac{r_m^{\frac{n}{2}}}{2\mu}\left\{\left[\kappa+\frac{n}{2}+(-1)^n\right]\cos\frac{n\theta_m}{2}-\frac{n}{2}\cos\frac{(n-4)\theta_m}{2}\right\}g_{n,m}\\
&= \frac{-r_m^{\frac{n}{2}}}{2\mu}\left\{\left[\kappa+\frac{n}{2}-(-1)^n\right]\sin\frac{n\theta_m}{2}-\frac{n}{2}\sin\frac{(n-4)\theta_m}{2}\right\}h_{n,m}\\
&= \frac{r_m^{\frac{n}{2}}}{2\mu}\left\{\left[\kappa-\frac{n}{2}-(-1)^n\right]\sin\frac{n\theta_m}{2}+\frac{n}{2}\sin\frac{(n-4)\theta_m}{2}\right\}l_{n,m}\\
&= \frac{r_m^{\frac{n}{2}}}{2\mu}\left\{\left[\kappa-\frac{n}{2}+(-1)^n\right]\cos\frac{n\theta_m}{2}+\frac{n}{2}\cos\frac{(n-4)\theta_m}{2}\right\}
\end{aligned}
\tag{17}
$$

$$
\begin{Bmatrix} u_1 \\ \vdots \\ u_m \\ v_1 \\ \vdots \\ v_m \end{Bmatrix} =
\begin{bmatrix}
1 & f_{1,1}\cdots f_{n,1} & 0 & g_{1,1}\cdots g_{n,1} & -r_1\sin\theta_1 \\
\vdots & \vdots & \vdots & \vdots & \vdots \\
1 & f_{1,m}\cdots f_{n,m} & 0 & g_{1,m}\cdots g_{n,m} & -r_m\sin\theta_m \\
0 & h_{1,1}\cdots h_{n,1} & 1 & l_{1,1}\cdots l_{n,1} & r_1\cos\theta_1 \\
\vdots & \vdots & \vdots & \vdots & \vdots \\
0 & h_{1,m}\cdots h_{n,m} & 1 & l_{1,m}\cdots l_{n,m} & r_m\cos\theta_m
\end{bmatrix}
\begin{Bmatrix} a_0 \\ a_1 \\ \vdots \\ a_n \\ b_0 \\ b_1 \\ \vdots \\ b_n \\ R \end{Bmatrix}
\tag{18}
$$

where m is the data point index. a_0 and b_0 are used to compensate for the rigid body motion. R compensates for the rigid body rotation.

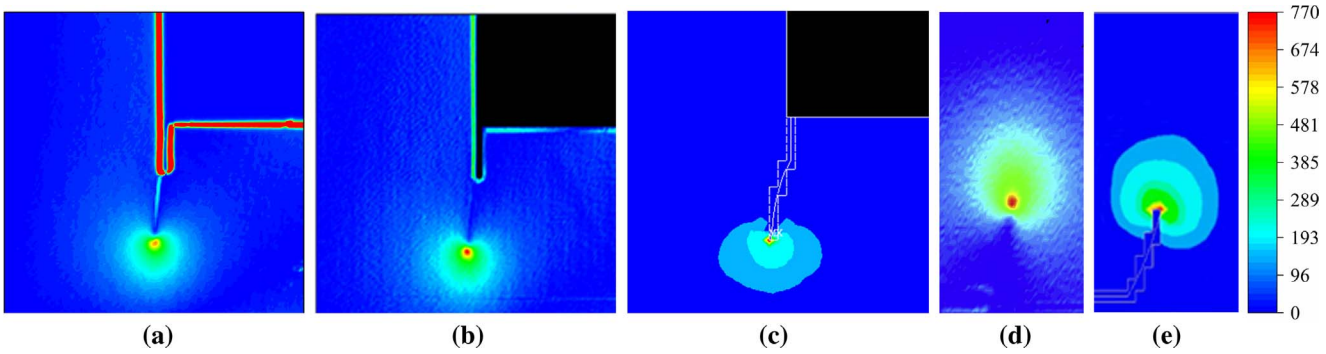

Fig. 17. The sum of principal stresses change(MPa): (a) without MC in load type 2, (b) with MC in load type 2, (c) XFEM result in load type 2, (d) with MC in load type 1 and (e) XFEM result in load type 1.

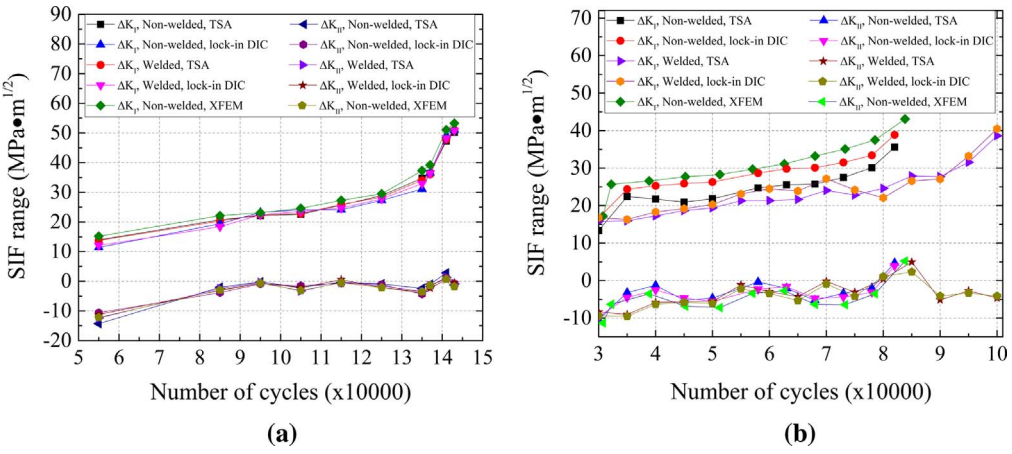

Fig. 18. Change in SIF range with number of cycles. (a) load type 1, (b) load type 2.

By selecting data points around the crack tip (Fig. 13) and performing regression analysis, these unknown parameters can be determined. The SIF of mode I and II can then be calculated from Eq. (19).

$$K_I = a_1\sqrt{2\pi}, K_{II} = -b_1\sqrt{2\pi} \tag{19}$$

The displacement range fields of the two test rigs in horizontal direction and vertical direction at 135,000 cycles and 78,000 cycles are presented in Figs. 14 and 15 respectively. In here, the lock-in DIC result and XFEM result are compared. It is obvious that the displacement fields of two methods fit well which means the lock-in DIC result is precise and can be used to evaluate SIF.

The local strain field around the crack tip was assessed with a subset size of 21 × 21 pixels with a step size of 5 px. In the ε_x data shown in Fig. 16 at 135,000 cycles and 78,000 cycles respectively, the strain concentrations at the end of the crack is clearly visible. Spurious strains shown in grey color are generated at the crack due to the discontinuity and associated large displacement across the crack.

5.2.2. SIF evaluation approach by TSA

For the calculation of the SIF from thermoelastic images, an initial estimation for the crack tip is required which is based on the phase change along the crack. Data points are then collected from the crack tip region. It is worth noting that points are selected from the region where the validity of the mathematical model is assured. Using regression analysis, the SIF can be inferred by employing Stanley's methodology [29]:

$$\Delta(\sigma_1 + \sigma_2) = \frac{2\Delta K_I}{\sqrt{2\pi r}}\cos\left(\frac{\theta}{2}\right) - \frac{2\Delta K_{II}}{\sqrt{2\pi r}}\sin\left(\frac{\theta}{2}\right) \tag{20}$$

The edge effect caused by calculations of the temperature difference between the specimen surface and the background can affect the temperature distribution of infrared images significantly. To obtain accurate stress field of TSA, the motion compensation(MC) technique was employed using the method proposed by Wang [30]. Fig. 17 shows the sum of principal stresses change without MC, with MC and XFEM result. It is clear that the maximum sum of principal stresses change happens on the edge of the specimen before MC. However, after MC, the edge effect has been minimised so that the contour map of TSA result is smoothed and the maximum sum of principal stresses happens on the crack tip area rather than the edge. Futhermore, the TSA result after MC and the XFEM result are very close.

5.2.3. SIF comparison

The SIF values of mode I and mode II obtained from different specimens, different techniques and different load types are shown in Fig. 18. From both Fig. 18(a) and (b), all of the SIF values of mode I are larger than that of mode II, which means mode I is the dominant crack growth form in both of the load types. The overall trend of mode I SIF is increasing while the trend of mode II SIF is fluctuant. Furthermore, the SIF range values of mode I predicted by XFEM are larger than the experimental results of specimens. Interesting conclusion is that both the experimental methods well agree with good approximation with themselves, while also the theoretical values are in good agreement.

5.2.4. Error evaluation of regression analysis

The SIF values from lock-in DIC and TSA all date from regression analysis. As a result, the displacement fields of lock-in DIC and the sum of principal stresses of TSA can be recalculated. Fig. 19 shows the reconstructed horizontal displacement range fields and vertical displacement range fields in load type 1 and load type 2. The fitted data is of good quality to the experimental displacement fields since the fitted contour lines are smoother than the experimental lines.

To do a regression analysis for TSA data, 15 points at each key cycle were selected around the crack tip. According to Eq. (20), the sum of

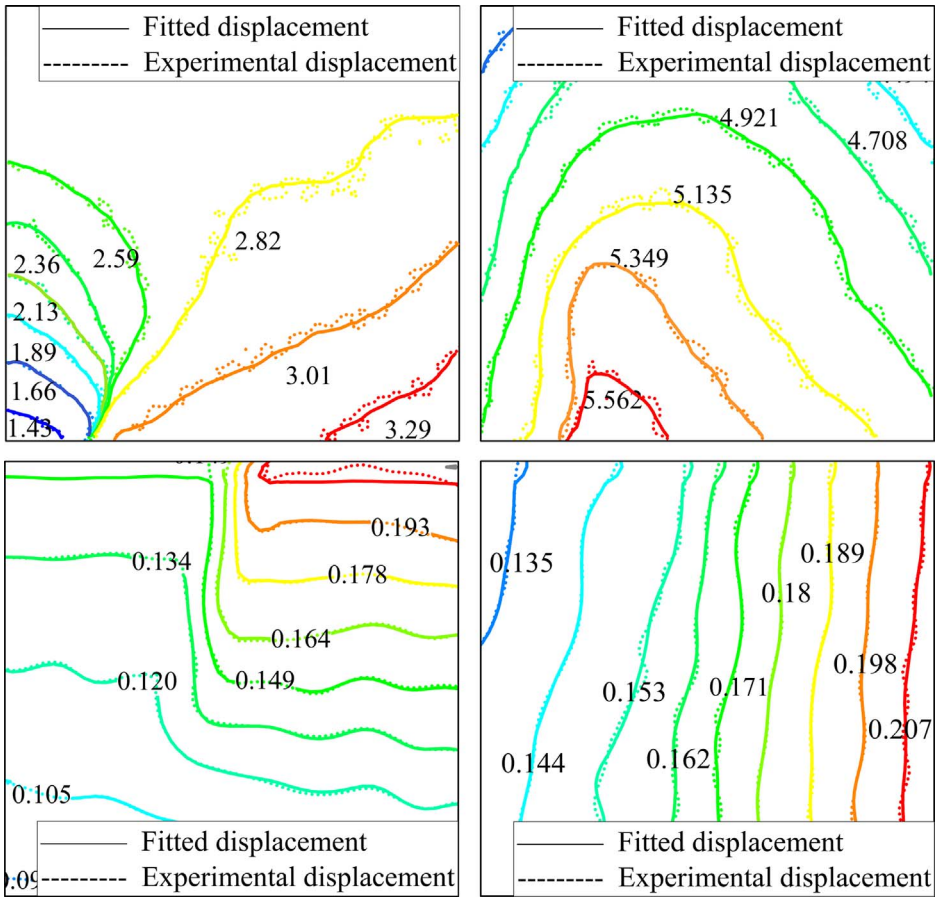

Fig. 19. Experimental and fitted displacement range fields around the crack tip. (a) Horizontal displacement range in load type 1, (b) vertical displacement range in load type 1, (c) horizontal displacement range in load type 2 and (d) vertical displacement range in load type 2.

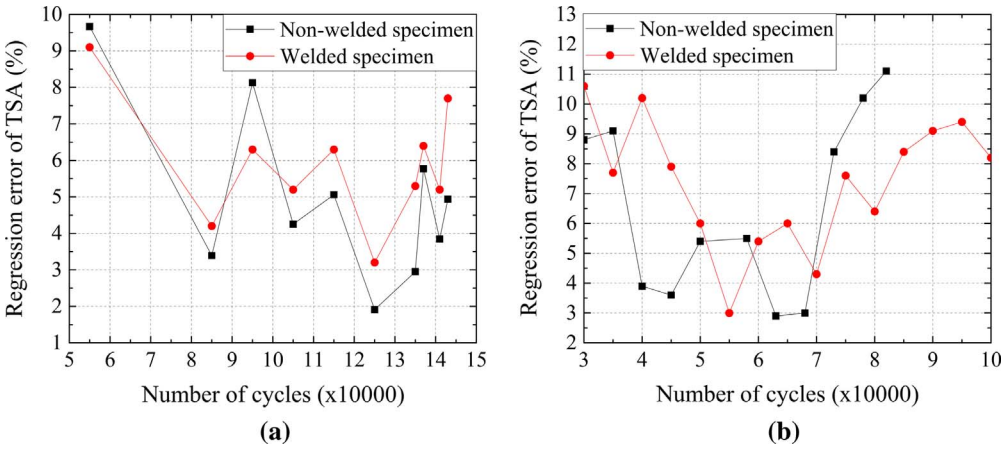

Fig. 20. Regression error evaluation of TSA (a) load type 1, (b) load type 2.

principal stresses were recalculated for each selected point. Hence the averaged regression analysis error can be calculated at each key cycle. Fig. 20 indicates the averaged regression error of TSA at each key cycle. The errors of the non-welded specimen and welded specimen are relatively large at the beginning and the ending of the cycle. The errors are relatively small at the middle stage of cycles.

5.3. Paris' Law constants using data fitting

The Paris' Law equation can be transformed into the following format

$$\log(da/dN) = m\log(\Delta K) + \log C \tag{21}$$

For each test rig experiment, the Paris Law constants can be determined using data fitting since the SIF values were evaluated at different crack lengths. Fig. 21 shows the scatter plot and linear fit line for each test rig experiment. The fitted equations and the corresponding Paris' Law constants are attached to the figures.

By using the newly determined Paris' Law constants, a new XFEM simulation was conducted. Fig. 22 shows the change in crack length with number of cycles for non-welded specimen, welded specimen and XFEM. It is clear that the XFEM curve fits well with the experimental results before 60,000 cycles. The cracks of non-welded specimen and welded specimen grow in a faster speed after 60,000 cycles since the curves are getting steeper and steeper. According to Paris' Law, this means the crack propagation is in the third stage, that is the unstable propagation stage. However, the XFEM curve keeps increasing in a linear trend after 60,000 cycles. The reason is that XFEM algorithm in

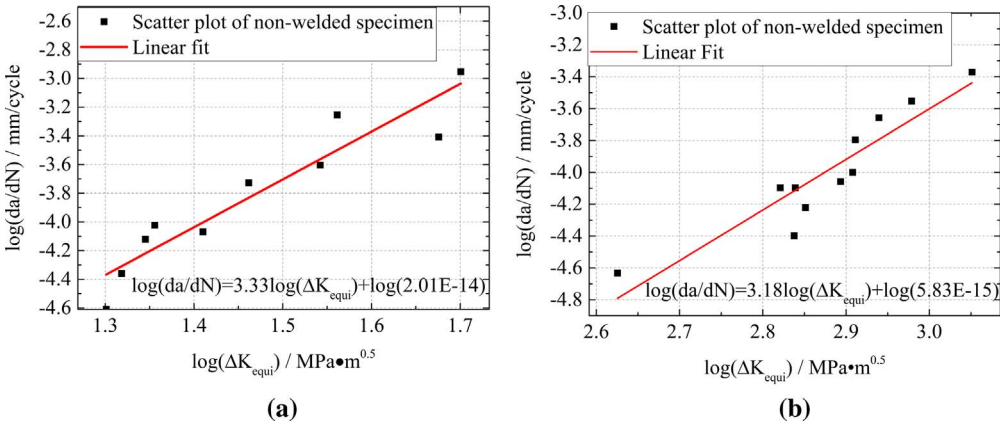

Fig. 21. Paris' Law fitting (a) load type 1, (b) load type 2.

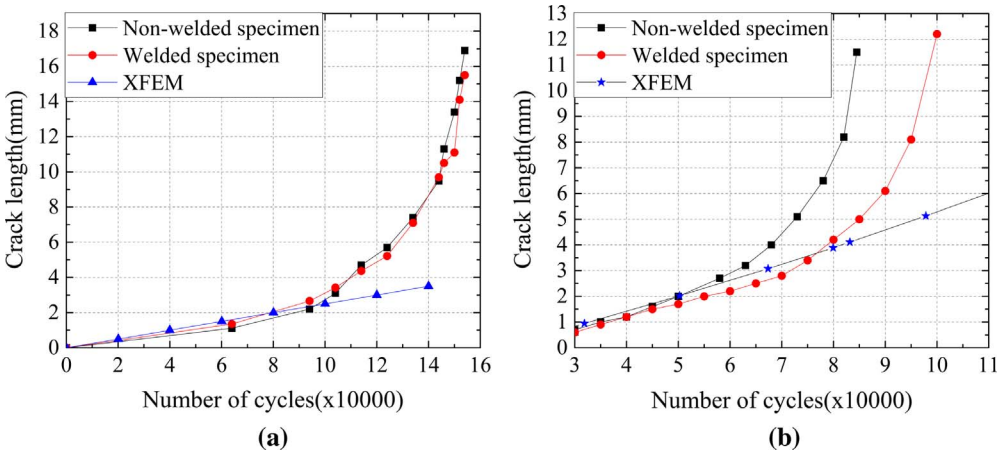

Fig. 22. Change in crack length with number of cycles by using corrected Paris' Law constants (a) load type 1, (b) load type 2.

ANSYS is based on the linear region of Paris' Law.

6. Conclusions

Fatigue crack growth was measured on welded and non-welded specimens made of 316L stainless steel in two types of test rig. For this purpose, lock-in DIC and TSA were employed to monitor the crack propagation progress. The following conclusions can be drawn:

(a) The low frame rate capability of standard digital cameras can also be used in the application of DIC at high loading rates since the lock-in algorithm can effectively be applied to strain and displacement data obtained using DIC.
(b) All of the SIF values of mode I are larger than that of mode II, which means mode I is the dominant crack growth form in both of the load types. The overall trend of mode I SIF is increasing while the trend of mode II SIF is fluctuant. Furthermore, the SIF range values of mode I predicted by XFEM are larger than the experimental results of specimens.
(c) The reconstructed horizontal displacement range fields and vertical displacement range fields in load type 1 and load type 2 show good quality comparing to the experimental displacement fields.
(d) The maximum sum of principal stresses change happens on the edge of the specimen before MC. However, after MC, the edge effect is minimised so that the contour map of TSA result is smoothed and the maximum sum of principal stresses happens on the crack tip area rather than the edge. The TSA result after MC and the XFEM result are very close which means the motion compensation method can significantly improve the accuracy of TSA.
(e) Paris' Law constants which are determined using the experimental results can be employed to correct the XFEM simulation. All of the results such as crack growth path, displacement field and SIF show good agreement with the experimental data.

Acknowledgements

This research has been sponsored by the National Key Research and Development Program of China (grant numbers 2016YFB1200404-08, 2016YFB1200602-07), the Fundamental Research Funds for the Central Universities (grant number 2016YJS130) and China Scholarship Council (CSC).

References

[1] La Rosa G, Clienti C, Marino Cugno Garrano A. The use of digital image correlation to correct the thermoelastic curves in static tests. Volume 2, Procedia Structural Integrity; 2016. p. 2140–7.
[2] Kirugulige MS, Tippur H, Denney T. Measurement of transient deformations using digital image correlation method and high-speed photography: application to dynamic fracture. Appl Opt 2007;46(22):5083–96.
[3] Chao YJ, Luo PF, Kalthoff JF. An experimental study of the deformation fields around a propagating crack tip. Exp Mech 1998;38(2):79–85.
[4] Gonzales GLG, Gonzalez JAO, Castro JTP. A J-integral approach using digital image correlation for evaluating stress intensity factors in fatigue cracks with closure effects. Theor Appl Fract Mec 2017;90:14–21.
[5] Fruehmann RK, Dulieu-Barton JM, Quinn S. The use of a lock-in amplifier to apply digital image correlation to cyclically loaded components. Opt Lasers Eng 2015;68:149–59.
[6] Stanley P, Chan WK. Quantitative stress analysis by means of the thermoelastic effect. J Strain Anal 1985;20:129–37.
[7] Farahani Behzad V, Tavares Paulo J, Moreira PMGP. SIF determination with thermoelastic stress analysis. Volume 2, Procedia Structural Integrity; 2016. p. 2148–55.
[8] Yates JR, Zanganeh M, Tomlinson RA, Brown MW, Diaz Garrido FA. Crack paths under mixed mode loading. Eng Fract Mech 2008;75:319–30.
[9] Wu SC, Xiao TQ, Withers PJ. The imaging of failure in structural materials by synchrotron radiation X-ray microtomography. Int J Fatigue 2017;182:127–56.
[10] Wu P, Ifju P. Flapping wing structural deformation and thrust correlation study with

flexible membrane wings. AIAA J 2012;48:2111–22.
[11] Risbet M, Feissel P, Roland T, Brancherie D, Roelandt J-M. Digital image correlation technique: application to early fatigue damage detection in stainless steel. Proc Eng 2010;2:2219–27.
[12] Shannon CS. Communication in the presence of noise. Proc IEEE 2000;88:569–87.
[13] Temple PA. An introduction to phase sensitive amplifiers: an inexpensive student instrument. Am J Phys 1975;43:801–7.
[14] Scofield JH. Frequency-domain description of a lock-in amplifier. Am J Phys 1975;62:129–33.
[15] Gaspar J, Chen SF, Gordillo A, Hepp M, Ferreyra P, Marques C. Digital lock-in amplifier: study, design and development with a digital signal processor. Microprocess Microsy 2004;28:157–62.
[16] Harwood N, Cummings WM. Thermoelastic stress analysis. Bristol: IOP Publishing; 1991.
[17] Tomlinson RA, Patterson EA. Examination of crack tip plasticity using thermoelastic stress analysis. Thermomechanics and Infra-Red Imaging, Volume 7, Conference Proceedings of the Society for Experimental Mechanics Series; 2011. p. 123–9.
[18] Shih CF, Moran B, Nakamura T. Energy release rate along a three-dimensional crack front in a thermally stressed body. Int J Fract 1986;30:79–102.
[19] Suresh S. Fatigue of materials. 2nd ed. Cambridge: Cambridge University Press; 1998.
[20] Paris PC, Gomez MP, Anderson WP. TA rational analytic theory of fatigue. Trend Eng 1961;13:9–14.
[21] Erdogan F, Sih GC. On the crack extension in plates under plane loading and transverse shear. J Basic Eng 1963;85:519–27.
[22] Peixoto Daniel FC, de Castro Paulo MST. Mixed mode fatigue crack propagation in a railway wheel steel. XV Portuguese Conference on Fracture; 2016. p. 150–7.
[23] Ganesh P, Kaul R, Sasikala G, Kumar H, Venugopal S, Tiwari P. Fatigue crack propagation and fracture toughness of laser rapid manufactured structures of AISI 316L stainless steel. Metallogr Microstruct Anal 2014;3:36–45.
[24] Peng X, Kulasegaram S, Bordas SPA, Wu SC. An extended finite element method (XFEM) for linear elastic fracture with smooth nodal stress. Comput Struct 2017;179:48–63.
[25] Maeng WY, Kang YH. Creep-fatigue and fatigue crack growth properties of 316LN stainless steel at high temperature. In: Transactions of the 15th international conference on structural mechanics in reactor technology (SMiRT-15) Seoul, Korea; 1999. p. 197–204.
[26] Suzuki K, Fukakura J, Kashiwaya H. Near-threshold fatigue crack growth of 316L stainless steel at liquid helium temperature. J Soc Mater Sci, Jpn 1989;38:1309–15.
[27] Ioannou Angelos Nikolaos. Evaluation of stresses in welded ship structure. Southampton: University of Southampton; 2013.
[28] Williams ML. On the stress distribution at the base of a stationary crack. J Appl Mech 1957;27:109–14.
[29] Stanley P, Chan WK. The determination of stress intensity factors and crack tip velocities from thermoelastic infra-red emissions. In: Proceedings of International Conference of Fatigue of Engineering Materials and Structures, c262, ImechE, Sheffield, UK; 1986. p. 105–14.
[30] Wang W, Fruehmann RK, Dulieu-Barton JM. Application of digital correlation to reduce the effect of complex motions in thermoelastic analysis. Strain 2015;51:405–18.